

**Macroscopic plastic deformation through an integrated first-principles calculations and  
finite element simulations: Application to nickel single crystal**

Shipin Qin<sup>1</sup>, Shun-Li Shang<sup>1</sup>, John Shimanek<sup>1</sup>, Zi-Kui Liu<sup>1</sup>, and Allison M. Beese<sup>1,2,\*</sup>

<sup>1</sup>*Department of Materials Science and Engineering, The Pennsylvania State University,  
University Park, PA 16802, USA*

<sup>2</sup>*Department of Mechanical Engineering, The Pennsylvania State University, University Park,  
PA 16802, USA*

*\* Corresponding author: amb961@psu.edu*

**Abstract:**

The crystal plasticity finite element method (CPFEM) has been widely adopted to describe mechanical properties of single crystals. Even though CPFEM explicitly considers the deformation mechanisms of single crystals, the parameters used within the CPFEM framework are typically determined through fitting of macroscopic experimental results. In the present work, a multiscale approach that combines first-principles calculations of individual phases and CPFEM is proposed to predict the strain hardening behavior of pure Ni single crystal. Density functional theory (DFT)-based first-principles calculations were used to predict the strain hardening behavior on the slip systems of Ni single crystal in terms of the flow resistance of dislocations calculated from ideal shear strength and elastic properties. The DFT-based predictions based on pure edge and pure screw dislocations provided parameter inputs for a CPFEM framework. Actual plastic deformation of pure Ni is more complex, initially involving edge dislocations, and eventually also the interactions of edge dislocations that result in junctions with screw dislocation characters.

Hence, a model that combines influences of both edge and screw dislocations was proposed. It was found that CPFEM predictions based solely on edge dislocations agreed well with experiments at small strains ( $< 0.06$  in the present work), while the predictions adopting the proposed edge-screw model fully captured experimental data at large deformations.

**Keywords:** Crystal plasticity; Single crystal deformation; Multi-scale modeling; First-principles calculations; Flow resistance

## 1. Introduction

Due to their high ductility, the mechanical properties of face-centered cubic (fcc) single crystals have been widely investigated, providing insight into the mechanisms of their plasticity at different deformation stages. The mechanical response of single crystals is typically described in the literature by the resolved shear stress-strain behavior on particular slip systems within the single crystal [1]. Pure Ni single crystal is one such example, whose mechanical properties have been investigated through both experiments [2–4] and simulations [5,6].

Prior experimental work on Ni single crystal has focused on determining the resolved shear stress-strain behavior on its slip systems. For example, Haasen [2] performed tension tests on Ni single crystal wire along different orientations, and at different temperatures, and revealed an orientation-independent inverse relationship between the initial critical resolved shear stress (CRSS, represented by  $\tau_0$  in the present work) and temperature.

The crystal plasticity finite element method (CPFEM) was developed based on the understanding of plastic deformation of crystals through slip mechanisms, and has been viewed as a promising approach for modeling the mechanical behavior of single crystals [7]. CPFEM models have been used to capture experimentally observed mechanical behavior of single crystals and polycrystals [8–12]. The often-numerous parameters in CPFEM models can be determined through fitting of macroscopic experimental curves, using lower length-scale computations, or a combination of the two. While fitting macroscopic experimental curves is purely phenomenological, combination with lower length-scale calculations generally considers the underlying physical mechanisms. Widely used lower length-scale computational methods include dislocation dynamics [13–17] and molecular dynamics [18–20]. However, additional assumptions are often required when determining the CPFEM model parameters through dislocation dynamics

or molecular dynamics, which may diminish the connection between the fitted parameters and their physical meaning. For example, in the dislocation dynamics framework in Li et al. [17], the authors assumed that the mobility of a screw dislocation is a small constant fraction of that of an edge dislocation and that the evolution of dislocation density can be fully described by the six mechanisms they considered.

Beyond the classical mechanics used in molecular and dislocation dynamics, density functional theory (DFT)-based first-principles calculations provide a description of atomic processes based on the electronic configuration of atoms. However, few efforts have been made to combine DFT-based methods with CPFEM models, mainly due to their low computational efficiency and the prohibitively large supercells required to explicitly model dislocations. Advanced techniques have developed to account for far-field strains more efficiently while maintaining atomistic accuracy near the dislocation core [21–23], but complex interactions of large numbers of dislocations remain firmly out of reach of first-principles methods. More commonly, first-principles methods consider a defect-free crystal to provide elastic constants while plasticity behavior is left to experimental calibration, as in the study by Ma et al. on Ti-Nb alloys [24].

Due to the limitations of DFT-based calculations, the present work makes no attempt to explicitly consider dislocations and instead presents a method of linking a computationally tractable problem, the ideal shearing process, to a realistic description of macroscopic deformation. By applying pre-strains in the first-principles calculations, the interaction between dislocations was considered, and the flow resistance for pure edge and pure screw dislocations in the presence of an elastic field was predicted using the Peierls-Nabarro model [25,26]. The CPFEM model parameters were determined from DFT-based predictions and were then adopted for predicting the macroscopic stress-strain curves of various single crystal tensile tests. Since screw dislocations

can cross-slip to get around obstacles, their contribution to strain hardening is less significant compared to that of edge dislocations when the obstacle density is low [27]. In pure metallic fcc single crystals, a low obstacle density corresponds to a low dislocation density (and thus low strain) as dislocations serve as the main obstacles. Therefore, CPFEM simulations for pure edge dislocations were first performed to predict the strain hardening behavior at small strains. At large strains, when the obstacle density becomes high and the contributions from screw dislocations need to be considered, a simple model is proposed to combine the DFT-based predictions of the two dislocation types. CPFEM simulations that consider both types of dislocations were performed to predict the strain hardening behavior at large strains.

## **2. Methodology**

### **2.1 Approach**

In a single fcc crystal, dislocations themselves are the main obstacles that inhibit dislocation movement and thus the major strain hardening mechanism [27,28]. In the small strain range, the dislocation density is very low, so the dislocation interaction is primarily long-range, meaning that dislocations interact with other dislocations through their elastic field [1]. In the large strain range, short-range dislocation interactions become the major strain hardening source because the dislocation density is high and the dislocation mean free path is low [27,29]. In short-range dislocation interactions, dislocation cores make contact with each other and form jogs or junctions. Jogs provide only modest strain hardening because, while dislocations can be pinned by jogs, they can still bow out to accommodate applied deformation. In contrast, junctions are usually very strong, and can lead to the formation of sessile dislocation segments. It is commonly accepted that junctions are the major source of strain hardening in stage II deformation of fcc crystals [27], and

in many modeling works, the model predictions considering only junctions have shown satisfactory agreement with experiments [27,30,31].

In DFT-based calculations, direct consideration of dislocations is challenging due to the high computational cost of the calculations, which limits their size, and the inherently extended nature of dislocations. Therefore, explicit first-principles calculations of dislocations have been made only with the help of elastic Green function solutions to account for the far-field elastic distortions, attenuating image forces due to periodic boundary conditions, and allowing the accurate yet expensive DFT-based calculations to relax only those atoms deemed to be part of the dislocation core [22,23,32,33]. In this work, a different approach is proposed to consider dislocations in an indirect manner. Specifically, the method adopted here relies on the improved analytic form to estimate Peierls stress proposed by Joós et al. [34], which is based mainly on ideal shear strength and elastic properties and is widely employed [35–38]. Physically, the Peierls stress is the flow resistance of a dislocation in a crystal. The ideal shear strength of crystals can be obtained from DFT-based calculations. When an elastic field is imposed on the model for the DFT-based calculations, the resulting ideal shear strength changes, which is indicative of the influence an elastic field has on the flow resistance. Since long-range dislocation interactions are achieved by elastic fields created by dislocations, the estimated flow resistance under an elastic field can then be interpreted as the influence of dislocation interactions on the flow resistance of a dislocation. A schematic summary of the approach is shown in Figure 1.

One of the central proposals of the current work is that the response of the ideal crystal to elastic strains contains information relevant to a description of macroscopic deformation. Strain applied to the ideal crystal in one direction is used to determine, through the Peierls-Nabarro equation, the stress required to move a single dislocation in an otherwise perfect lattice. Adding

strain in an orthogonal in-plane direction increases the difficulty of the ideal shear process, analogously to the way strain field interactions of multiple dislocations increase the difficulty of their motion through a realistic crystal.

## 2.2 Crystal plasticity model

The crystal plasticity framework presented by Huang [39] is adopted in the current work. In this framework, strain hardening is described as the evolution of the CRSS on one slip system due to the shear strain on any slip system:

$$\dot{\tau}_c^\alpha = \sum_{\beta=1}^l h_{\alpha\beta} |\dot{\gamma}^\beta| \quad \text{Eq. 1}$$

where  $\tau_c^\alpha$  is the CRSS on slip system  $\alpha$ ,  $\gamma^\beta$  is the shear strain on slip system  $\beta$ , and  $h_{\alpha\beta}$  is the hardening matrix. Many forms of  $h_{\alpha\beta}$  have been proposed, while a form presented by Peirce et al. [40] is adopted in the present work for its minimal number of parameters, the simplicity of its mathematical form, and the physical interpretability of the individual parameters. The strength of the chosen hardening model, while simple and less physically-motivated than the model of Taylor based on dislocation density [41], is its ability to interface with other models without relying on explicit descriptions of dislocations that would be prohibitive in first-principles methods due to the computational expense. The models of Taylor [41] and Peirce et al. [40] describe the same deformation response and therefore must also describe the effects of collective dislocation motion, whether explicitly considered or not. Peirce et al. [40] proposed that:

$$h_{\alpha\beta} = q_{\alpha\beta} \left[ h_0 \operatorname{sech}^2 \left| \frac{h_0 \gamma}{\tau_s - \tau_0} \right| \right] \quad \text{Eq. 2}$$

where

$$q_{\alpha\beta} = \begin{cases} 1, & \alpha = \beta \\ 1.4, & \alpha \neq \beta \end{cases} \quad \text{Eq. 3}$$

characterizes the difference between self-hardening ( $\alpha = \beta$ ) and latent hardening ( $\alpha \neq \beta$ ). With this form, the slip system level strain hardening curve increases monotonically with a decreasing slope and approaches a saturation value asymptotically. The initial slope of this curve is controlled by  $h_0$ , the saturation value is controlled by  $\tau_s$ , and  $\tau_0$  is the initial CRSS value.

In the above model, the parameters to be determined are: the initial CRSS,  $\tau_0$ ; the initial strain hardening behavior at small strains,  $h_0$ ; and the strain hardening saturation behavior at large strains,  $\tau_s$ . In the present study, the first two parameters were predicted through DFT-based computations, while  $\tau_s$  was taken from results reported in the literature. In addition to the above, the elastic constants  $c_{ij}$  (Mandel notation) are also needed. For an fcc lattice there are only three independent elastic constants:  $c_{11}$ ,  $c_{12}$ , and  $c_{44}$ . These constants were also predicted through DFT-based computations.

### 2.3 First-principles calculations of flow resistance

In the model described above, the initial CRSS,  $\tau_0$ , is the minimum shear stress required to initiate plastic deformation [42]. For perfect crystal lattices without any defects, this corresponds to the ideal shear strength  $\tau_{IS}$ , while for crystal lattices with pre-existing dislocations, this corresponds to the flow resistance  $\tau_f$ . The current study aims to predict the strain hardening behavior at room temperature in single crystals in which dislocations are present, therefore,  $\tau_0$  corresponds to the flow resistance  $\tau_f$ , which is predicted using first-principles calculations. The initial strain hardening behavior, or  $h_0$ , can be taken from the  $\tau_f$  values as a function of strain. In



the current study, the evolution of flow resistance is calculated by applying increasing values of pre-strain to the lattice in the DFT-based calculations.

It should be noted that all DFT-based calculations of CRSS in the present work were performed at 0 K for simplification, while all experimental data were taken at room temperature. This simplification is appropriate because, for pure metals, the CRSS values at 0 K are close to those at room temperature [43]. Additionally, previous calculations have indicated that properties from DFT-based calculations at 0 K are comparable to experimental data measured at room temperature (298 K) for many properties. For example, the predicted difference of enthalpy of formation is negligible between 0 K and room temperature ( $< 0.2$  kJ/mol for metal sulfides [44]), the predicted bulk moduli of Ni and Ni<sub>3</sub>Al decrease about 9 GPa (5 %) from 0 K to room temperature [45], and the predicted ideal shear strength of Ni decreases about 0.1 GPa (2 %) [46].

In the present work, the flow resistance,  $\tau_f$ , is estimated using the Peierls-Nabarro model [25,26] as shown in Eq. 4 for a wide dislocation [34], where dislocations in fcc metals fall into the category of wide dislocations because the distortions around them spread over a large volume [47].

$$\tau_p = \frac{Kb}{a} \exp(-2\pi z/d) \quad \text{Eq. 4}$$

Here,  $b$  is the Burgers vector,  $a$  is the row spacing of atoms within the slip plane (for example,  $a = a_0\sqrt{6}/4$ , where  $a_0$  is the lattice parameter, for the case of  $\{111\}\langle 11\bar{2} \rangle$  shear deformation of an fcc lattice), and  $\zeta$  is the half-width of the dislocation, given as:

$$z = \frac{Kb}{4\pi\tau_{IS}} \quad \text{Eq. 5}$$

where  $\tau_{IS}$  is the ideal strength. The elastic factor,  $K$ , is direction-dependent for an anisotropic crystal like that of pure Ni. For example, for an edge dislocation aligned with the  $z$ -direction, with

a Burgers vector  $\mathbf{b} = (b_x, b_y, 0)$ , the corresponding  $K_{e_x}$  of edge dislocation along the  $x$ -direction is given by [48],

$$K_{e_x} = (\bar{c}'_{11} + c'_{12}) \left[ \frac{c'_{66}(\bar{c}'_{11} - c'_{12})}{(\bar{c}'_{11} + c'_{12} + 2c'_{66})c'_{22}} \right]^{1/2} \quad \text{Eq. 6}$$

where  $\bar{c}'_{11} = (c'_{11}c'_{22})^{1/2}$  and  $c'_{ij}$  indicates the transformed elastic constants onto the slip system of interest. In the present work, the transformed lattice vectors of fcc Ni are parallel to the  $[11\bar{2}]$ ,  $[\bar{1}10]$ , and  $[111]$  directions of the conventional fcc lattice, i.e., the  $\mathbf{a}_{\text{orth}}$  ( $x$ ),  $\mathbf{b}_{\text{orth}}$  ( $y$ ), and  $\mathbf{c}_{\text{orth}}$  ( $z$ ) directions, respectively; see Figure 2a. Notably  $K_{e_x} = K_{e_y} (= K_e)$  for edge dislocations along the  $x$ - and  $y$ -directions for the present fcc Ni represented by the orthorhombic cell as shown in Figure 2a. The elastic factor for screw dislocations,  $K_s$ , of an anisotropic crystal is given by [48],

$$K_s = [c'_{44}c'_{55} - (c'_{45})^2]^{1/2} \quad \text{Eq. 7}$$

The ideal shear strength in Eq. 5 can be predicted directly by pure alias shear – a deformation similar to the dislocation motion that constitutes slip [46,49,50]. Alias shear involves only one sliding layer ( $n = 1$ ) with the atoms in other layers initially remaining in their original positions [46,49,50]; see Figure 2b. The relaxations of a pure alias shear include all degrees of freedom of a supercell except for the fixed shear angle as well as other constraints such as the pre-strain deformation discussed below.

Considering the major slip system in fcc lattices of  $\{111\}\langle 110 \rangle$  as well as the splitting of the  $1/2[\bar{1}10]$  dislocation into two Shockley partials on the (111) plane via  $1/2[\bar{1}10] \rightarrow 1/6[\bar{2}11] + 1/6[\bar{1}2\bar{1}]$  [46,48,50], a 6-atom orthorhombic supercell was adopted for fcc Ni with its lattice vectors  $\mathbf{a}_{\text{orth}}$ ,  $\mathbf{b}_{\text{orth}}$ , and  $\mathbf{c}_{\text{orth}}$  of the respective lengths  $0.5\sqrt{6}a_0$ ,  $0.5\sqrt{2}a_0$ , and  $\sqrt{3}a_0$  ( $a_0$  is the lattice

parameter of fcc Ni) parallel to the  $[11\bar{2}]$ ,  $[\bar{1}10]$ , and  $[111]$  directions, respectively; see Figure 2a. After  $\{111\}\langle 11\bar{2}\rangle$  alias shear, the deformed lattice vector matrix  $\mathbf{A}'$  is given as:

$$\mathbf{A}' = \mathbf{A}\mathbf{F} \quad \text{Eq. 8}$$

where  $\mathbf{A}$  is the undeformed lattice vector matrix and  $\mathbf{F}$  is the deformation matrix, given as:

$$\mathbf{F} = \begin{bmatrix} 1 & 0 & 0 \\ 0 & 1 & 0 \\ \gamma_{112} & \gamma_{110} & 1 \end{bmatrix} \quad \text{Eq. 9}$$

where  $\gamma$  is the magnitude of the engineering shear strain, i.e., the ratio of shear displacement to the height of the supercell [46,49],  $\gamma_{112}$  is the shear strain along the  $[11\bar{2}]$  direction, and  $\gamma_{110}$  is the pre-strain along the  $[\bar{1}10]$  direction. Note that the pre-strain along  $[\bar{1}10]$  creates an elastic field in the model, analogous to that created by dislocations, as discussed in Section 2.1, while the shear strain long  $[11\bar{2}]$  allows DFT-based calculations to probe the maximum ideal shear strength on the partial slip system. Thus, the above operations can be interpreted as probing the dependence of  $\tau_{IS}$  on the elastic field created by dislocations in the crystal lattice.

Elastic properties can be predicted by computing stresses under given strains by means of first-principles calculations and Hooke's law, as previously shown [51,52]. The imposed strains used here to predict the single crystal elastic constants,  $c_{ij}$ , are  $\pm 0.007$  and  $\pm 0.013$ . Using the above (Eq. 4 to Eq. 7), the single crystal flow resistances were predicted under the presence of elastic fields created by other dislocations for both an edge and a screw dislocation, the character of which depended solely on the version of the adopted elastic factor  $K$ . Details of the first-principles calculations, for both elastic properties and flow resistance, may be found in the appendix.

### 3. Results and discussion

#### 3.1 Results from first-principles calculations

##### 3.1.1. Ideal shear strength of fcc Ni with and without pre-strain

Table 1 summarizes the predicted ideal shear strengths of fcc Ni by pure alias shear deformation along  $\{111\}\{11\bar{2}\}$  without pre-strain, i.e.,  $\gamma_{110} = 0$  (see Eq. 9). It shows that the fewer the number of  $\{111\}$  layers (represented by  $n_{111}$  in the present work), the larger the  $\tau_{IS}$ . The maximum  $\tau_{IS} = 5.15$  GPa for the case of  $n_{111} = 3$ . This  $\tau_{IS}$  value (5.15 GPa) agrees well with previous predictions around 5.0 GPa using pure alias or pure affine shear deformations [46]. The current value also agrees reasonably well with the value estimated from nanoindentation of approximately  $8 \pm 1.5$  GPa [53], with the difference likely due to the measurement being performed on a non-close packed (001) plane [53] and the stabilizing effect of the triaxial stress state beneath the indenter tip [54]. With increasing  $n_{111}$ , the predicted  $\tau_{IS}$  decreased significantly (for example,  $\tau_{IS} = 2.603$  GPa when  $n_{111} = 9$ ) despite the fact that the absolute displacement distance increased slightly (from 0.780 to 0.798 Å; see Table 1). By considering the limited layers involved in the movement of dislocation cores during experimental slip processes and the experimental estimate of  $\tau_{IS} \sim 8 \pm 1.5$  GPa, the minimum value of  $n_{111} = 3$  and the corresponding  $\tau_{IS} = 5.15$  GPa were selected for further investigation in the present study.

To understand the decrease of  $\tau_{IS}$  with increasing  $n_{111}$ , the stretching force constants are plotted in Figure 3 with phonon calculations for two fcc-based orthorhombic lattices: one with 3 layers (6 atoms) and one with 6 layers (12 atoms) after pure alias shear with the same amount of displacement distance (0.5 Å) applied. Here the force constants, particularly the dominant stretching force constants shown in Figure 3 (as opposed to the significantly smaller bending force

constants), provide quantitative understanding of the interaction or bonding between atomic pairs [55,56]. A large and positive force constant indicates strong bonding, while a negative force constant suggests the pair of atoms tend to separate from each other. Figure 3 shows that the maximum stretching force constants from the 3-layer lattice are higher than those from the 6-layer lattice (2.46 versus 2.28 eV/Å<sup>2</sup>), indicating the bonding between atoms becomes weaker with an increasing number of {111} layers during pure alias shear deformation, which results in lower  $\tau_{IS}$  values.

Table 2 shows that the predicted  $\tau_{IS}$  increases and  $\gamma_{112}$  decreases with increasing pre-strain,  $\gamma_{110}$  (see Eq. 9). As discussed in Section 2.1, the  $\gamma_{110}$  pre-strain created a strain field on the close packed plane analogous to that created by slipping, thus allowing the DFT-based predictions to be interpreted as the change of flow resistance ( $\tau_f$ ) on one slip system due to the shear strain on another slip system. The  $\tau_{IS}$  values increased from 5.15 to 5.26 GPa as  $\gamma_{110}$  increased from 0 to 0.049, indicating that the existence of pre-strain makes the {111}{11 $\bar{2}$ } shear deformation slightly more difficult (Table 2).

### 3.1.2. Elastic properties of fcc Ni with and without pre-strain

Table 3 summarizes the predicted elastic constants of fcc Ni in terms of the 6-atom orthorhombic cell ( $c'_{ij,orth}$ ). Note that by adopting the relationship given by Hirth and Lothe [48],  $c'_{ij,orth}$  can be transformed to  $c_{ij,cub}$ , which are the elastic constants in terms of the 4-atom conventional cubic cell to be compared to experimental data. These predictions (pre-strain  $\gamma_{110} = 0$ ) agree with the experimental elastic constants extrapolated to 0 K [57]. With increasing pre-

strain  $\gamma_{110}$  (up to 0.049), Table 3 shows that the  $c'_{ij,orth}$  values remain almost constant under these small  $\gamma_{110}$  values; for example,  $c'_{11,orth} = 338 \sim 341$  GPa.

### 3.1.3. Flow resistance $\tau_f$ of fcc Ni with and without pre-strain

In the present study, the flow resistance was calculated using Eq. 4, with the elastic factor  $K$  being calculated using Eq. 6 (for edge dislocations) and Eq. 7 (for screw dislocations). Further, each version of  $K$  may be calculated by either considering or disregarding the local strain fields imposed at each level of pre-strain through the adoption of pre-strain dependent or independent elastic constants. In the present study, all calculations of  $K$  accounted for pre-strain. Since the flow resistance deals only with local deformations as a single dislocation moves the distance of one Burgers vector, elastic properties describing local stress and strain fields are more appropriate than bulk elastic properties calculated without considering any pre-strain. Moreover, by considering pre-strain in the calculation of the elastic factor, each input value of Eq. 4 is calculated using the same initial (pre-strained) simulation conditions.

Table 2 summarizes the predicted flow resistance ( $\tau_f$  values) of all four versions at 0 K, compared with experimental  $\tau_0$  values at room temperature [2,3,58,59]. The predicted  $\tau_f$  values of edge dislocations (9.4 MPa with  $\gamma_{110} = 0$ ) agree well with experimental  $\tau_0$  values (5.5 to 19.6 MPa [2,3,58–64]), but those of screw dislocations (117.7 to 308.7 MPa with  $\gamma_{110} = 0$ ) are significantly higher than experiments. While there are arguments as to which type of dislocations dominate in the small strain range [65,66], it is known that screw dislocations are able to cross-slip to get around obstacles, which, in pure Ni single crystal, are the dislocations themselves. Therefore, in the small strain range when the dislocation density is low, dislocation segments of majority edge

character are more likely than their screw-type counterparts to be responsible for the strain hardening of the material. Xia and El-Azab [13] also showed that the flow strength and strain hardening rate were significantly reduced in the small strain range when cross-slipping was enabled in their model. With increasing  $\gamma_{110}$  pre-strain, the predicted  $\tau_P$  values increase. For example,  $t_f^{edge}$  increased from 9.4 to 11.1 MPa (increase of about 18 %) as  $\gamma_{110}$  increased from 0 to 0.049. The increase of  $\tau_f$  stems mainly from the increase of  $\tau_{IS}$  compared to elastic properties (see Eq. 4 and values in Table 2).

### 3.2 CPFEM model parameters from first-principles calculations

In above, the prediction of flow resistance was made by assuming pure edge or pure screw dislocations. However, as detailed above, the contributions to strain hardening should come from both types of dislocations except in the small strain range, where hardening can be approximated as originating from edge-type dislocation segments only. Therefore, the present study first attempts to predict the mechanical behavior at small deformations when edge dislocations dominate. At large deformations, the predictions based on pure edge and pure screw dislocations must be combined to consider the influence of both types of dislocations, which will be discussed in Section 3.5.

As discussed in Section 2, DFT-based calculations predicted the flow resistance of a dislocation gliding along slip system  $\alpha$  under the influence of an elastic field from other dislocations. The intensity of the elastic field can be characterized by the pre-strain imposed in the DFT-based calculations. This pre-strain also corresponds to the local effect of the shear strain on a latent slip system caused by the long-range elastic field of dislocations and is the  $\gamma^\beta$  ( $\alpha \neq \beta$ )

in Section 2.2. By imposing different levels of pre-strain, the relationship between  $\tau_c^\alpha$  and  $\gamma^\beta$  was predicted (i.e.,  $\tau_f$  versus  $\gamma_{110}$  in Table 2). In this case, Eq. 1 through Eq. 3 can be simplified as:

$$\dot{\tau}_c^\alpha = 1.4 \left[ h_0 \operatorname{sech}^2 \left| \frac{h_0 \gamma^\beta}{\tau_s - \tau_0} \right| \right] |\dot{\gamma}^\beta|, (\alpha \neq \beta) \quad \text{Eq. 10}$$

where  $h_0$ ,  $\tau_0$ , and  $\tau_s$  are model parameters. By matching the relationship between  $\tau_c^\alpha$  and  $\gamma^\beta$  determined from Eq. 10 (note that  $\tau_c^\alpha = \tau_0$  when  $\gamma^\beta = 0$ ) with that predicted in DFT-based calculations, the values of  $\tau_0$  and  $h_0$  were determined, as shown in Figure 4. Note that DFT-based predictions are limited to only small strains where  $h_0$  and  $\tau_0$  play a dominant role, so a value reported in the literature was adopted for  $\tau_s$  (40 MPa [5]). The determined parameter values are summarized in Table 4.

### 3.3 Experimental results in the literature

To show the predictive accuracy of the present approach, models of Ni single crystal tensile tests from the literature incorporated the hardening parameters determined above into the CPFEM framework to evaluate macroscopic stress-strain responses. The experiments considered in the present work include two uniaxial tension tests reported by Haasen [2] on 99.999% purity Ni wire specimens with a diameter of 2.24 mm and a length of 71.12 mm, and a uniaxial tension test reported by Yao et al. [64] on 99.999% purity Ni specimens with a gauge section size of  $2.5 \times 5.5 \times 0.25 \text{ mm}^3$ , both for single crystals. Figure 5a provides the resolved shear stress-strain curves reported in these publications [2,64]. Note that the loading directions with respect to the crystal orientation are different for each test, i.e.,  $\langle \bar{1} 5 10 \rangle$  and  $\langle \bar{1} 2 8 \rangle$  by Haasen [2], and  $\langle 011 \rangle$  by Yao et al. [64]. The process of calculating engineering values from the resolved shear stress-strain



curves is detailed in Appendix B, with the final engineering stress-strain curves shown as Figure 5b.

Discrepancies in the reported literature on pure Ni single crystal CRSS and flow behavior stem from differences in material purity, initial dislocation density, and potential experimental uncertainties. A method must therefore be adopted to evaluate these differences so that they may be considered when comparing computational results to experimental data. Here, differences in experimental results were evaluated by comparing their initial CRSS values since the value of the CRSS is independent of the assumptions adopted for converting force-displacement data to resolved shear-stress strain data.

Figure 6 shows the initial CRSS value of pure Ni reported by ten different groups [2,3,58–64,67]. Since the value reported by Latanision et al. [67] is significantly higher than the other reported values, it was excluded from evaluation in the present study. The rest of the experimental data all lie between 5 MPa and 20 MPa, and the statistics of these data are shown in Table 5. According to the statistical analysis of the initial CRSS reported by nine different groups over more than 80 years, the experimental data in the literature exhibited a relative error of 43%.

### **3.4 DFT-based CPFEM predictions at small strains**

To simulate the tests reported in the literature, the full geometry of the specimens in each test was modeled. All of the specimens were discretized with 0.2 mm hexahedral full integration elements (element type C3D8 [68]) in the gauge region, and the models contain 20,590 elements for the wire specimen by Haasen [2] and 2,176 elements for the dogbone specimen by Yao et al. [64]. In both models, the vertical movement of the bottom nodes was constrained while a uniform vertical displacement was applied to the top nodes. The horizontal movements of all top and

bottom nodes of the flat dogbone specimen in Yao et al.'s study were also constrained to avoid potential out-of-plane distortion [69]. The crystal plasticity model was implemented in the commercial finite element software ABAQUS through a user subroutine UMAT [68] originally developed by Huang [39,70].

Figure 7 shows the simulated engineering stress-strain curves compared to the respective experimental results. Comparisons were made in the small strain range only because the CPFEM predictions considered only edge dislocations, as discussed in Section 3.2. Error bars of 43% were added to the stress strain curves, corresponding to the standard deviation of initial CRSS values reported in the literature and discussed above.

As can be seen from Figure 7, the initial yield stresses in all of the tests were reasonably predicted, supporting the approximation of considering only edge dislocations in the small strain range. Table 6 provides a detailed comparison between experimental and predicted initial yield stresses for all tests. At small strains, the flow stress was reasonably approached by the CPFEM predictions, as the predictions were within the error range up to 10% strain for Haasen's test along the  $\langle \bar{1} 5 10 \rangle$  direction and for Yao et al.'s test, and up to 6% strain for Haasen's test along the  $\langle \bar{1} 2 8 \rangle$  direction.

### **3.5 Modeling and predictions at large strains**

As discussed in Section 3.2, the DFT-based predictions based on pure edge and pure screw dislocations need to be combined to accurately predict the strain hardening behavior of fcc metals at large strains. This is also in accordance with the fact that in the large strain range, dislocations come into contact and form junctions that often exhibit screw character [19,71–73]. It was reported that these junctions contribute most to the strain hardening of fcc crystals in the large strain range

[27]. Kubin et al. [74] considered junctions formation to be a result of mobile dislocations reacting with the stored forest dislocations and showed through derivation that the junction density in fcc crystals increases with shear strain on slip systems. Through discrete dislocation dynamics simulations, Guruprasad and Benzerga [75] and Huang et al. [76] reported the same trend in junction density. This indicates that the contribution of screw dislocations to strain hardening increases with plastic strain. Therefore, in the present study, the following model is proposed to account for the increasing influence of screw components to strain hardening with plastic strain, combining first-principles results based on pure edge and pure screw dislocations:

$$\tau_c^{\alpha,es} = (1 - w\gamma^\beta)\tau_f^{edge} + w\gamma^\beta\tau_f^{screw} \quad \text{Eq. 11}$$

where  $w$  is a weighting factor that controls the contribution from each type of dislocation,  $\gamma^\beta$  is the shear strain on slip system  $\beta$ ,  $\tau_f^{edge}$  and  $\tau_f^{screw}$  are the predicted CRSS in the DFT-based calculations (see Eq. 4) for pure edge and pure screw dislocations, respectively, and  $\tau_c^{\alpha,es}$  is the CRSS on slip system  $\alpha$  (see Eq. 1) considering contributions to the strain hardening from both edge and screw dislocations. Both  $\tau_f^{edge}$  and  $\tau_f^{screw}$  change with  $\gamma^\beta$ . By including  $\gamma^\beta$  in the model, the influence of both types of dislocations are included naturally: (1) edge dislocations are dominant at small strains ( $\tau_c^{\alpha,es} = \tau_f^{edge}$  when  $\gamma^\beta = 0$ ), and (2) the influence of screw dislocations increases with increasing strain, in accordance with the studies of Kubin et al. [74], Guruprasad and Benzerga [75] and Huang et al. [76].

An inverse method based on the experimental data from ref. [64] was used to determine the weighting factor  $w$  in Eq. 11. Figure 8 shows that the CPFEM simulations agreed well with experiments over the full experimental strain range with  $w = 0.33$ . Note that Eq. 11 produced a new resolved shear stress-strain curve, based on which a new set of  $\tau_0$  and  $h_0$  values were

determined. Specifically,  $h_0$  is a function of the weighting factor,  $w$ , and its value reflects the contributions from both the edge dislocations and the screw dislocations based on the slope of the relationship given in Eq. 11. The new parameter values are summarized in Table 4. As discussed in Section 3.2, the saturation stress ( $\tau_s$  in Eq. 2) cannot be determined from DFT-based calculations; therefore,  $\tau_s$  was calibrated to be 300 MPa based on the experimental data in Figure 8b. Note that the value of  $\tau_s$  only affects the stress strain curve in the large strain range. In the present study, we performed a simulation with the  $\tau_s$  being an order of magnitude higher than 300 MPa, and the resultant stress-strain curve was only slightly different for engineering strains greater than 0.6. Therefore, the excellent agreement in Figure 8 and 8 is primarily attributed to the value of  $h_0$ , which is derived from the DFT-based calculation predictions and the weighting factor  $w$ .

To better evaluate the model, the strain hardening rate in the simulations were compared with those in experiments, as shown in Figure 8c. Since the experimental data were extracted from the literature, the strain hardening rate was not directly available and was estimated by fitting the engineering stress-strain curve with a 3rd order polynomial function and then taking its derivative. The figure shows that the CPFEM prediction well captured the estimated experimental strain hardening rate.

The wire tension tests performed by Haasen [2] were simulated again using the newly determined parameters that consider the influence of both edge and screw dislocations with plastic deformation. Figure 9a and c show that in the new CPFEM predictions of Haasen's tests, the flow stress agrees with the experimental results up to large strains. In Figure 9b and d, the strain hardening rate is compared (the experimental strain hardening curves were estimated in the same way as in Figure 8c). While the CPFEM predictions agreed well with the experimental strain hardening rate along  $\langle \bar{1} 5 10 \rangle$ , the experimental strain hardening rate along  $\langle \bar{1} 2 8 \rangle$  was not well

captured, despite the stress-strain curve being in good agreement in this direction. In general, the above shows that, even though DFT-based predictions were made for pure edge and/or pure screw dislocations, the effect of both types of dislocations can be combined through Eq. 11 to capture experimental stress-strain responses of single crystals under uniaxial tension at finite deformation.

It is emphasized that in the above predictions, only the weighting factor  $w$  was fitted from a macroscopic stress strain curve ( $\tau_s$  is disregarded as its contribution to the agreement is negligible, as explained above), while all other parameters were predicted from DFT-based calculations. In contrast, existing physics-based crystal plasticity models generally feature large numbers of fitting parameters, with the fitting process in practice diminishing the physical significance of each parameter. Moreover, Eq. 11 represents the limited assumptions made in the above approach to describe the behavior of dislocations, while dislocation density-based approaches rely on numerous assumptions across different length scales.

#### **4. Conclusions**

In the present work, a multiscale approach has been proposed to predict the macroscopic stress-strain behavior of pure Ni single crystal. Instead of calibrating CPFEM model parameters solely using macroscopic experimental results, the present CPFEM simulations employed DFT-based first-principles calculations of flow resistance at 0 K in terms of the predicted ideal shear strength and elastic properties. The conclusions of the present work are:

- The present DFT-based calculations of pure alias shear deformation indicated that the calculated ideal shear strength of fcc Ni (and other materials) is layer-dependent, decreasing with increasing atomic layers due to the decreased bonding between atoms, as revealed by phonon calculations.

- Through the application of increasing orthogonal in-plane shear strains, the increasing ideal shear stress along the main strain direction was computed. This elastic pre-strain in a perfect crystal is analogous to the strengthening effects of long-range strain fields between real dislocations and serves as a linkage between atomistic and continuum descriptions of hardening.
- Initial values of the flow resistance based on pure edge dislocation elastic factors at 0 K matched well with experimental critical resolved shear stress values at room temperature. This agrees with established theory on the ease with which edge dislocations move in fcc materials to accommodate initial plastic strain.
- Incorporating into the CPFEM framework the calculated flow resistance with several pre-strains, again based on pure edge elastic factors, resulted in a stress-strain prediction that agreed well with experimental results for small strains.
- A simple model for CPFEM parameters is proposed that combines the contributions to flow resistance from edge and screw dislocations as a function of strain, in agreement with the concept that junctions and less-mobile dislocation segments remain after an initial amount of plastic deformation accomplished by segments of edge character. With this combination, the present work accurately predicts the strain hardening of Ni single crystal through large deformations.

## **ACKNOWLEDGMENTS**

This work was financially supported by the U. S. Department of Energy (DOE) via award no. DE-FE0031553 and the Office of Naval Research (ONR) via contract no. N00014-17-1-2567. First-principles calculations were carried out partially on the ACI clusters at the Pennsylvania State

University, partially on the resources of NERSC supported by the DOE Office of Science under contract no. DE-AC02-05CH11231, and partially on the resources of XSEDE supported by NSF via grant no. ACI-1548562.

## **DATA AVAILABILITY**

All relevant data are available from the authors.

## Appendix A. Details of first-principles calculations

All DFT-based first-principles calculations in the present work were performed by the Vienna *Ab initio* Simulation Package (VASP) [77]. The ion-electron interaction was described by the projector augmented wave (PAW) method [78]; the exchange-correlation functional was depicted by the generalized gradient approximation (GGA, PW91) as parameterized by Perdew et al. [79]; and the core configuration of [Ar] was employed for Ni as recommended by VASP. In VASP calculations, the  $k$ -point meshes of  $10 \times 16 \times 7$  were used for the 6-atom orthorhombic supercell (see Figure 2a); the cutoff energy of 337 eV (i.e., the precision of “high” used in VASP) was employed for the plane-wave basis set; and the energy convergence criterion of electronic self-consistency was selected as  $10^{-5}$  eV per supercell for all calculations. The reciprocal-space energy integration was performed by the Methfessel-Paxton [80] technique with a 0.2 eV smearing width, which can result in accurate total energies as well as stresses. Concerning pure alias shear deformation, an external optimizer GADGET developed by Bučko et al. [81] was used to control both stresses and forces acting on each atom during VASP calculations. The relaxed stresses (except for the shear stresses due to the fixed  $\gamma_{112}$  and/or  $\gamma_{110}$  values) were less than 0.15 GPa, and the forces acting on atoms were less than 0.03 eV/Å. Spin polarization was considered in all first-principles calculations due to the magnetic nature of Ni.

Aiming toward understanding layer-dependent ideal shear strength, ancillary DFT-based calculations of pure alias shear along  $\{111\}\{11\bar{2}\}$  were also performed using the 6-atom (3-layer), 12-atom (6-layer), and 18-atom (9-layer) orthorhombic supercells based on the structure shown in Figure 2a. The corresponding  $k$ -point meshes were  $10 \times 16 \times 7$ ,  $9 \times 16 \times 3$ , and  $7 \times 12 \times 2$ , respectively. In addition, phonon calculations were also carried out to explore the origin of layer-dependent  $\tau$  in terms of the 6-atom (3-layer) and the 12-atom (6-layer) orthorhombic cells after  $\{111\}\{11\bar{2}\}$



pure alias shear by applying the same amount of shear displacement (0.5 Å). These phonon calculations were performed by the supercell approach [82] as implemented in the YPHON code [83,84]. The VASP code was again the computational engine in calculating force constants by the density functional perturbation theory. For both the 3-layer and the 6-layer orthorhombic lattices, the 72-atom supercells together with the  $3 \times 3 \times 2$   $k$ -point meshes were used for phonon calculations. Note that all other conditions used for these ancillary first-principles calculations were the same as the aforementioned settings.

## Appendix B. Interpretation of experimental data in the literature

In the works of Yao et al. [64] and Haasen [2], both of which were used for comparison purposes in Section 3.3 and beyond, the authors showed only the resolved shear stress and resolved shear strain data. However, it is not straightforward to convert directly measurable quantities in the tests, namely force and displacement, to resolved shear stress and resolved shear strain on slip systems; the conversion process depends on the assumptions made as discussed below [85].

In the work by Yao et al. [64], only one slip system was assumed to be operating. The resolved shear strain  $\gamma$  and the resolved shear stress  $\tau$  under this assumption are calculated as [69,86,87]:

$$\gamma = \frac{1}{\cos \theta_0} \left[ \sqrt{(1 + \varepsilon^{eng})^2 - \sin^2 \lambda_0} - \cos \lambda_0 \right] \quad \text{Eq. B12}$$

$$\tau = \sigma^{eng} \frac{\cos \theta_0}{1 + \varepsilon^{eng}} \sqrt{(1 + \varepsilon^{eng})^2 - \sin^2 \lambda_0} \quad \text{Eq. B13}$$

where  $\theta_0$  is the initial angle between the loading direction and the slip plane normal direction,  $\lambda_0$  is the initial angle between the loading direction and the slip direction,  $\sigma^{eng}$  is the engineering stress, and  $\varepsilon^{eng}$  is the engineering strain. This approximation assumes that the loading axis continually rotates with respect to the active slip system throughout loading, which is unlikely to be true in finite deformation [1]. **Error! Reference source not found.** and **Error! Reference source not found.** were used to calculate the engineering stress-strain curve in the tests in ref. [64].

In the framework of double slip, the rotation of the loading axis with respect to the active slip system is assumed to cease when it reaches a specific orientation. Before reaching this orientation, single slip operates, and the equations above can be applied. After the rotation of the loading axis activates a conjugate slip system, the two slip systems are assumed to operate simultaneously with

the same hardening rate, rotating the loading axis along the slip system boundary until reaching a point of stable double glide that prevents further rotation [86]. If  $\mathbf{n}_1$  and  $\mathbf{n}_2$  are the unit normals of the two slip planes, and  $\mathbf{u}_1$  and  $\mathbf{u}_2$  are the unit vectors of the two slip directions, the resolved shear strain  $\gamma$  and resolved shear stress  $\tau$  under the double glide approximation can be calculated as [86,88]:

$$\gamma = \frac{2}{\mathbf{n}_1 \mathbf{u}_2} \ln \left[ 1 + \frac{\mathbf{n}_1 \mathbf{u}_2}{|\mathbf{w}|} \frac{\sin \beta_0}{\cos \theta_0} (\cot \beta - \cot \beta_0) \right] \quad \text{Eq. B14}$$

$$\tau = \sigma^{eng} \frac{|\mathbf{w}|}{2} \cos \beta \left\{ \cos \theta_0 + \frac{\mathbf{n}_1 \mathbf{u}_2}{|\mathbf{w}|} \sin \beta_0 (\cot \beta - \cot \beta_0) \right\} \quad \text{Eq. B15}$$

$$\sin \beta = \frac{\sin \beta_0}{1 + \varepsilon^{eng}} \quad \text{Eq. B16}$$

where  $\mathbf{w} = \mathbf{u}_1 + \mathbf{u}_2$ , and  $\beta_0$  is the angle between the loading direction and  $\mathbf{w}$  at the onset of double glide. **Error! Reference source not found.** through **Error! Reference source not found.** were adopted in the present work to calculate the engineering stress-strain curves in Haasen's tests, in which the initial loading direction was  $\langle \bar{1} 5 10 \rangle$  for crystal #6 and  $\langle \bar{1} 2 8 \rangle$  for crystal #18 in ref. [2]. In both tests, the  $\{111\}\langle \bar{1} 0 1 \rangle$  slip system was active first. It was assumed that when the loading direction rotated to  $\langle \bar{5} 5 14 \rangle$  for crystal #6 and to  $\langle \bar{2} 2 9 \rangle$  for crystal #18, double slip began and  $\{\bar{1} \bar{1} 1\}\langle 0 1 1 \rangle$  started to operate as an additional slip system. The engineering stress-strain curves for all three tests, calculated using the above equations [2,64], are shown in Figure 5b.

**Figures**

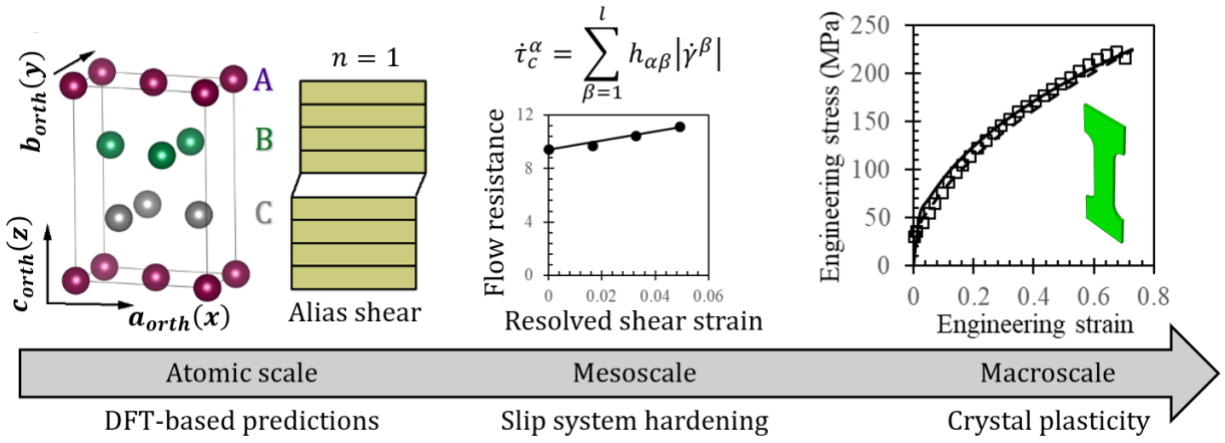


**Figure 1.** A schematic of the overall approach proposed in the current work, showing the transfer of information from the atomic scale ideal shear process to a mesoscale description of hardening on a slip system level to, finally, a description of macroscale deformation of single crystal samples.

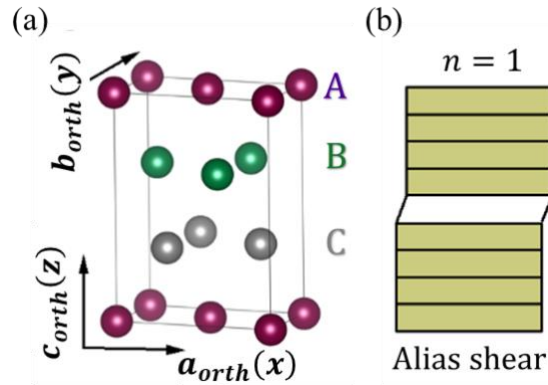


**Figure 2.** (a) Three-layer six-atom orthorhombic supercell of fcc lattice with its lattice vectors  $\mathbf{a}_{orth}(x)$ ,  $\mathbf{b}_{orth}(y)$ , and  $\mathbf{c}_{orth}(z)$  parallel to the  $[11\bar{2}]$ ,  $[\bar{1}10]$ , and  $[111]$  directions of the conventional fcc lattice; where the letters A, B, and C indicate three closed packed (111) planes. (b) Schematic diagrams of alias shear with atoms in only one plane involved in shear (i.e., the number of involved atomic planes,  $n$ , is one, shown as the unshaded area).

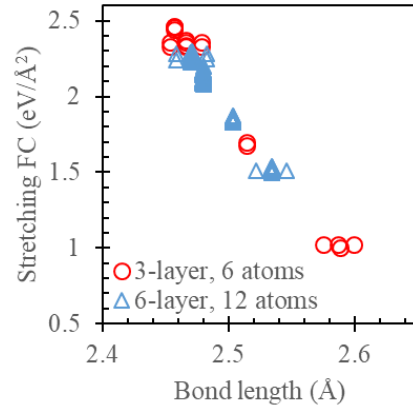


**Figure 3.** Stretching force constants (FCs) as a function of bond length for two fcc lattices of Ni: (i) the orthorhombic lattice with 3 layers and 6 atoms (see **Figure 2**), and (ii) the orthorhombic lattice with 6 layers and 12 atoms. Note that both lattices have the same shear displacement of 0.5 Å for the  $\{111\}\langle 11\bar{2}\rangle$  shear deformation, and the 72-atom supercells were employed for phonon calculations of both lattices.

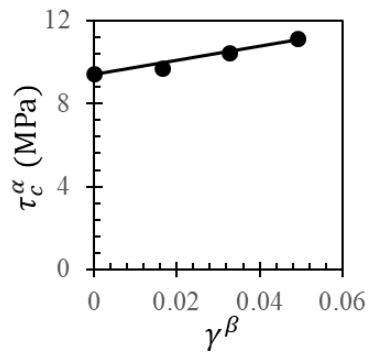


**Figure 4:** Critical resolved shear stress on slip system  $\alpha$  as a function of shear strain on slip system  $\beta$ . Symbols represent DFT-based predictions for edge dislocations, and lines show the corresponding CPFEM model curves.

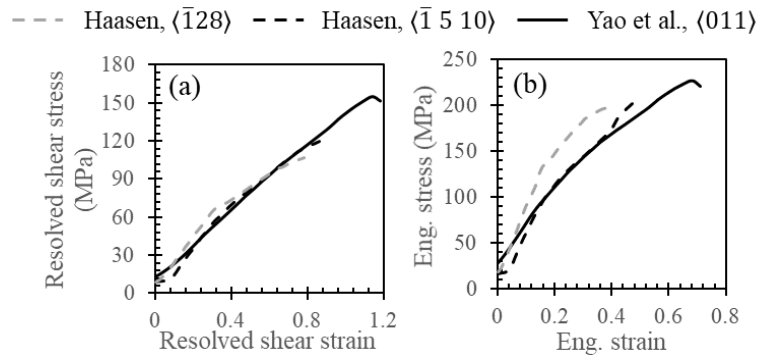
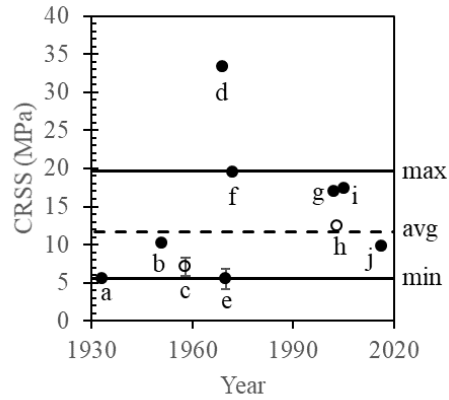


**Figure 5:** (a) Resolved shear stress vs. resolved shear strain and (b) engineering stress vs. engineering strain for pure Ni bulk single crystals in literature [2,64]. The crystallographic directions in the legend indicate the loading direction during the tests.





- a: Osswald (99.7 wt.% Ni) [58],
- b: Andrade et al. (99.9 wt.% Ni) [59],
- c: Haasen (99.999 wt.% Ni) [2],
- d: Latanision et al. (99.8 wt.% Ni) [67],
- e: Venkatesan et al. (unknown purity) [60],
- f: KondratEv et al. (99.999 wt.% Ni) [61],
- g: Hecker et al. (99.99 wt.% Ni) [62],
- h: Yao et al. (99.999 wt.% Ni) [64],
- i: Dimiduk et al., (unknown purity) [3],
- j: Luo et al. (99.99 wt.% Ni) [63].

**Figure 6:** Initial CRSS values of pure Ni reported in the literature. The value reported in ref. [67] was significantly higher than others and was excluded from the present study. The open symbols (c and h) correspond to the studies adopted in the present study for validation of CPFEM predictions.

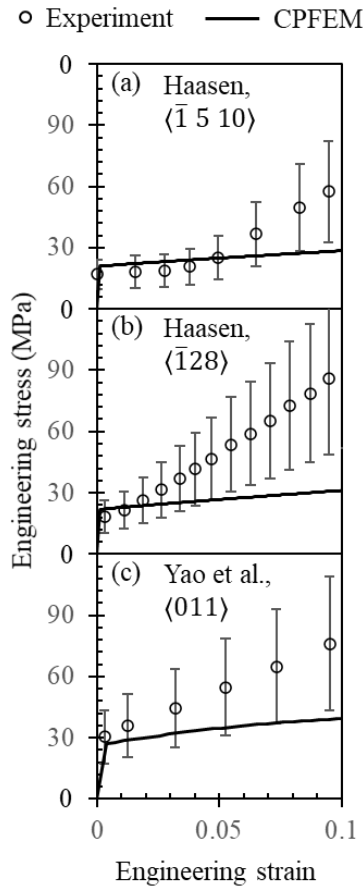


**Figure 7:** CPFEM predictions for (a,b) Haasen’s tests [2] and (c) Yao et al.’s test [64] from edge dislocation based flow resistance compared to experimental results (symbols) by Haasen et al. [2] and Yao et al. [64]. The error bars of 43% are based on the variance in CRSS values of pure Ni reported in the literature.

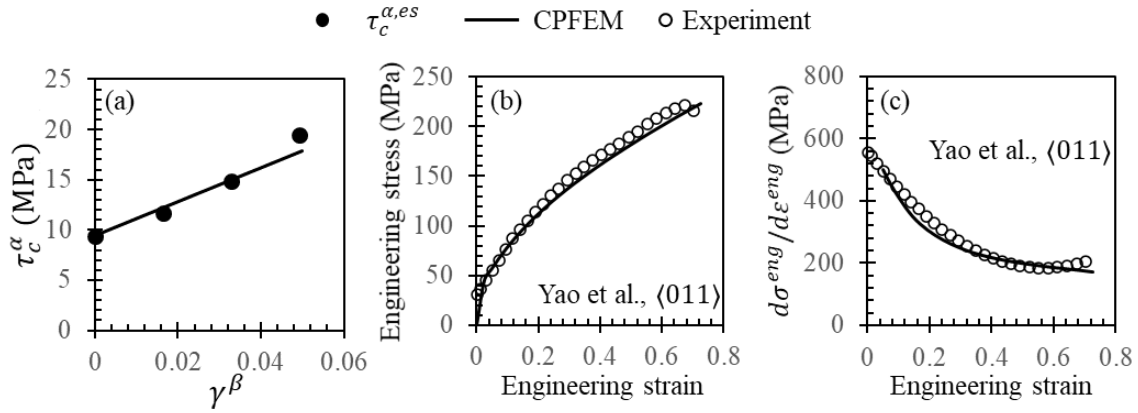


**Figure 8:** (a) Flow resistance,  $\tau_c^{\alpha,es}$ , on slip system  $\alpha$  that combines contributions from both edge and screw dislocations as a function of shear strain on slip system  $\beta$ . The calculated flow resistance are shown as symbols, and the corresponding CPFEM fits are also shown (lines). (b) CPFEM simulated engineering stress-strain curves (lines) of Yao et al.'s test [64] and the corresponding experimental results (symbols). (c) CPFEM simulated strain hardening rate (lines) of Yao et al.'s test [64] and the corresponding experimental results (symbols).

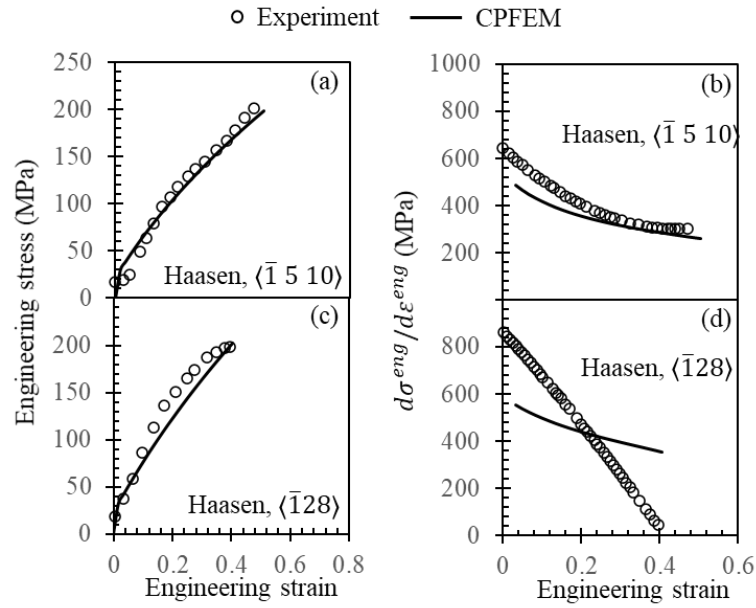


**Figure 9:** Engineering stress-strain curves (a,c) and strain hardening curves (b,d) for experiments (symbols) along (a,b)  $\langle \bar{1} 5 10 \rangle$  and (c,d)  $\langle \bar{1} 28 \rangle$  in ref. [2] compared to CPFEM predictions from the present study (lines) for the combined edge and screw predictions by DFT-based calculations (see Eq. 11).

## Tables

**Table 1.** Ideal shear strength ( $\tau_{IS}$ ), associated slip (displacement) distance on the shear plane, and engineering shear strain  $\gamma_{112}$  of fcc Ni due to pure alias shear along  $\{111\}\langle 11\bar{2}\rangle$  using supercells with different layers, with the total number of atoms within each supercell given.

Supercell	Slip distance (Å)	Shear strain $\gamma_{112}$	$\tau_{IS}$ (GPa)
3-layer (6 atoms)	0.78	0.13	5.15
6-layer (12 atoms)	0.80	0.07	3.61
9-layer (18 atoms)	0.80	0.04	2.60

**Table 2.** Ideal shear strength ( $\tau_{IS}$ ) of fcc Ni due to pure alias shear of  $\{111\}\langle 11\bar{2}\rangle$  with pre-strain  $\gamma_{110}$  along the  $[\bar{1}10]$  direction, together with the predicted flow resistance ( $\tau_f$ , MPa) at 0 K for edge and screw dislocations in comparison with experimental CRSS values ( $\tau_{CRSS}$ , MPa) at room temperature.

Properties	$\gamma_{110} = 0.000$	$\gamma_{110} = 0.016$	$\gamma_{110} = 0.033$	$\gamma_{110} = 0.049$
$\gamma_{112}$ <sup>a</sup>	0.128 (0.780)	0.126 (0.770)	0.124 (0.754)	0.120 (0.732)
$\tau_{IS}$ (in GPa)	5.15	5.16	5.19	5.26
$t_f^{edge}$ <sup>b</sup>	9.4	9.7	10.4	11.1
$t_f^{screw}$ <sup>b</sup>	308.7	318.6	362.1	457.5
$\tau_0$ (Expt.)	5.5 ~ 19.6 <sup>c</sup>			

<sup>a</sup> Engineering shear strain  $\epsilon_{112}$  corresponding to  $\tau_{IS}$ , where the slip distances (Å) on the shear plane are in the parentheses.

<sup>b</sup> By Eq. 4 with the input of  $\tau_{IS}$  in this Table,  $c_{ij}$  in Table 3, and lattice parameter  $a_0 = 3.52$  Å for fcc Ni from the present first-principles calculations.

<sup>c</sup> The range of CRSS values for Ni reported in [2,3,58–64]; see details in Figure 6.

**Table 3.** Calculated elastic constants (in GPa) of fcc Ni in terms of the conventional cubic lattice ( $c_{ij,\text{cub}}$ ) and the orthorhombic lattice ( $c'_{ij,\text{orth}}$ , see Figure 2a for the supercell) without and with pre-strain  $\gamma_{110}$ .

$c_{ij,\text{cub}}$ translated directly from $c'_{ij,\text{orth}}$ <sup>a</sup> $\begin{pmatrix} 265 & 161 & 161 & 0 & 0 & 0 \\ & 265 & 161 & 0 & 0 & 0 \\ & & 265 & 0 & 0 & 0 \\ & & & 127 & 0 & 0 \\ & & & & 127 & 0 \\ & & & & & 127 \end{pmatrix}$	
$c'_{ij,\text{orth}}$ without pre-strain $\gamma_{110} = 0.000$ $\begin{pmatrix} 340 & 137 & 113 & 0 & 32 & 0 \\ & 340 & 113 & 0 & -32 & 0 \\ & & 365 & 0 & 0 & 0 \\ & & & 79 & 0 & -32 \\ & & & & 79 & 0 \\ & & & & & 101 \end{pmatrix}$	$c'_{ij,\text{orth}}$ with pre-strain $\gamma_{110} = 0.016$ $\begin{pmatrix} 339 & 138 & 114 & 0 & 32 & -4 \\ & 339 & 114 & 0 & -32 & 0 \\ & & 367 & -8 & 0 & 6 \\ & & & 79 & 6 & -32 \\ & & & & 79 & 0 \\ & & & & & 102 \end{pmatrix}$
$c'_{ij,\text{orth}}$ with pre-strain $\gamma_{110} = 0.033$ $\begin{pmatrix} 338 & 137 & 113 & 0 & 31 & -9 \\ & 339 & 113 & 0 & -31 & 0 \\ & & 365 & -16 & 0 & 12 \\ & & & 78 & 12 & -31 \\ & & & & 78 & 0 \\ & & & & & 102 \end{pmatrix}$	$c'_{ij,\text{orth}}$ with pre-strain $\gamma_{110} = 0.049$ $\begin{pmatrix} 341 & 137 & 112 & -1 & 31 & -13 \\ & 341 & 112 & -1 & -31 & 1 \\ & & 365 & -23 & -2 & 17 \\ & & & 76 & 17 & -31 \\ & & & & 76 & 0 \\ & & & & & 102 \end{pmatrix}$

<sup>a</sup> Experimental elastic constants extrapolated to 0 K [57]:  $c_{11} = 261.2$ ,  $c_{12} = 150.8$ , and  $c_{44} = 131.7$  GPa.

**Table 4:** CPFEM parameter values (see Eq. 10), where  $c_{ij}$  are elastic constants of fcc Ni reported in Table 3. All of the parameters in this table were determined through DFT-based calculations in the present study, except  $\tau_s$  and  $w$ . The values for  $\tau_s$  were either taken from literature [5] (edge based) or calibrated from macroscopic experiments (edge screw mix), and  $w$  was calibrated from macroscopic experiments. See detailed discussion in Section 3.5.

	$c_{11}$ (GPa)	$c_{12}$ (GPa)	$c_{44}$ (GPa)	$h_0$ (MPa)	$\tau_0$ (MPa)	$\tau_s$ (MPa)	$w$
Edge based	265	161	127	24	9	40	-
Edge screw mix				120	9	300	0.33

**Table 5:** Statistics of the initial CRSS values in **Figure 6**. The outlier reported in ref. [67] is excluded.

Max	Min	Average	Std. Dev.	Relative error
19.6 MPa	5.5 MPa	11.66 MPa	5.01 MPa	43%

**Table 6:** Initial yield stresses (in MPa) from pure Ni single crystal tests by Haasen et al. [2] and Yao et al. [64] together with the corresponding CPFEM predictions in the present work.

Experimental value	Haasen, $\langle \bar{1} 5 10 \rangle$	Haasen, $\langle \bar{1} 28 \rangle$	Yao et al. $\langle 011 \rangle$
		17	19
CPFEM	21	22	27
Error compared to experiment	24%	18%	12%

## References

- [1] K. S. Havner, *Finite plastic deformation of crystalline solids*. Cambridge University Press, 1992.
- [2] P. Haasen, “Plastic deformation of nickel single crystals at low temperatures,” *Philos. Mag.*, vol. 3, no. 28, pp. 384–418, 1958.
- [3] D. M. Dimiduk, M. D. Uchic, and T. A. Parthasarathy, “Size-affected single-slip behavior of pure nickel microcrystals,” *Acta Mater.*, vol. 53, no. 15, pp. 4065–4077, Sep. 2005.
- [4] C. P. Frick, B. G. Clark, S. Orso, A. S. Schneider, and E. Arzt, “Size effect on strength and strain hardening of small-scale [1 1 1] nickel compression pillars,” *Mater. Sci. Eng. A*, vol. 489, no. 1–2, pp. 319–329, 2008.
- [5] X. Zhang and F. Shang, “A continuum model for intermittent deformation of single crystal micropillars,” *Int. J. Solids Struct.*, vol. 51, no. 10, pp. 1859–1871, 2014.
- [6] C. Keller, A. M. Habraken, and L. Duchene, “Finite element investigation of size effects on the mechanical behavior of nickel single crystals,” *Mater. Sci. Engng A*, vol. 550, pp. 342–349, 2012.
- [7] F. Roters, P. Eisenlohr, L. Hantcherli, D. D. Tjahjanto, T. R. Bieler, and D. Raabe, “Overview of constitutive laws, kinematics, homogenization and multiscale methods in crystal plasticity finite-element modeling: Theory, experiments, applications,” *Acta Mater.*, vol. 58, no. 4, pp. 1152–1211, Feb. 2010.
- [8] B. Eidel, “Crystal plasticity finite-element analysis versus experimental results of pyramidal indentation into (0 0 1) fcc single crystal,” *Acta Mater.*, vol. 59, no. 4, pp. 1761–1771, 2011.
- [9] C. Zambaldi, F. Roters, D. Raabe, and U. Glatzel, “Modeling and experiments on the indentation deformation and recrystallization of a single-crystal nickel-base superalloy,” *Mater. Sci. Eng. A*, vol. 454–455, pp. 433–440, 2007.
- [10] C. Keller, E. Hug, A. M. Habraken, and L. Duchene, “Finite element analysis of the free surface effects on the mechanical behavior of thin nickel polycrystals,” *Int. J. Plast.*, vol. 29, no. 1, pp. 155–172, 2012.



- [11] T. Ohashi, R. I. Barabash, J. W. L. Pang, G. E. Ice, and O. M. Barabash, “X-ray microdiffraction and strain gradient crystal plasticity studies of geometrically necessary dislocations near a Ni bicrystal grain boundary,” *Int. J. Plast.*, vol. 25, no. 5, pp. 920–941, May 2009.
- [12] S. Ghosh, A. Shahba, X. Tu, E. L. Huskins, and B. E. Schuster, “Crystal plasticity FE modeling of Ti alloys for a range of strain-rates. Part II: Image-based model with experimental validation,” *Int. J. Plast.*, vol. 87, pp. 69–85, 2016.
- [13] S. Xia and A. El-Azab, “Computational modelling of mesoscale dislocation patterning and plastic deformation of single crystals,” *Model. Simul. Mater. Sci. Eng.*, vol. 23, no. 5, p. 55009, 2015.
- [14] S. Xia, J. Belak, and A. El-Azab, “The discrete-continuum connection in dislocation dynamics: I. Time coarse graining of cross slip,” *Model. Simul. Mater. Sci. Eng.*, vol. 24, no. 7, p. 75007, 2016.
- [15] P. Lin and A. El-Azab, “Implementation of annihilation and junction reactions in vector density-based continuum dislocation dynamics,” *Model. Simul. Mater. Sci. Eng.*, vol. 28, no. 4, p. 45003, 2020.
- [16] A. Vattré, B. Devincre, F. Feyel, R. Gatti, S. Groh, O. Jamond, and A. Roos, “Modelling crystal plasticity by 3D dislocation dynamics and the finite element method: The Discrete-Continuous Model revisited,” *J. Mech. Phys. Solids*, vol. 63, no. 1, pp. 491–505, 2014.
- [17] D. Li, H. Zbib, X. Sun, and M. Khaleel, “Predicting plastic flow and irradiation hardening of iron single crystal with mechanism-based continuum dislocation dynamics,” *Int. J. Plast.*, vol. 52, pp. 3–17, 2014.
- [18] S. Groh, E. B. Marin, M. F. Horstemeyer, and H. M. Zbib, “Multiscale modeling of the plasticity in an aluminum single crystal,” *Int. J. Plast.*, vol. 25, no. 8, pp. 1456–1473, Aug. 2009.
- [19] V. Yamakov, D. Wolf, S. R. Phillpot, and H. Gleiter, “Dislocation-dislocation and dislocation-twin reactions in nanocrystalline Al by molecular dynamics simulation,” *Acta Mater.*, vol. 51, no. 14, pp. 4135–4147, 2003.

- [20] V. Bulatov, F. F. Abraham, L. Kubin, B. Devincre, and S. Yip, “Connecting atomistic and mesoscale simulations of crystal plasticity,” *Nature*, vol. 391, no. 6668, pp. 669–672, Feb. 1998.
- [21] D. R. Trinkle, “Lattice Green function for extended defect calculations: Computation and error estimation with long-range forces,” *Phys. Rev. B*, vol. 78, no. 1, p. 014110, Jul. 2008.
- [22] A. M. Z. Tan and D. R. Trinkle, “Computation of the lattice Green function for a dislocation,” *Phys. Rev. E*, vol. 94, no. 2, pp. 30–36, Aug. 2016.
- [23] Y. J. Hu, M. R. Fellingner, B. G. Bulter, Y. Wang, K. A. Darling, L. J. Kecskes, D. R. Trinkle, and Z. K. Liu, “Solute-induced solid-solution softening and hardening in bcc tungsten,” *Acta Mater.*, vol. 141, pp. 304–316, Dec. 2017.
- [24] D. Ma, M. Friák, J. Neugebauer, D. Raabe, and F. Roters, “Multiscale simulation of polycrystal mechanics of textured  $\beta$ -Ti alloys using ab initio and crystal-based finite element methods,” *Phys. Status Solidi*, vol. 245, no. 12, pp. 2642–2648, 2008.
- [25] F. R. N. Nabarro, “Fifty-year study of the Peierls-Nabarro stress,” *Mater. Sci. Eng. A*, vol. 234–236, pp. 67–76, Aug. 1997.
- [26] J. N. Wang, “Prediction of Peierls stresses for different crystals,” *Mater. Sci. Eng. A*, vol. 206, no. 2, pp. 259–269, Feb. 1996.
- [27] L. P. Kubin, B. Devincre, and M. Tang, “Mesoscopic modelling and simulation of plasticity in fcc and bcc crystals: Dislocation intersections and mobility,” *J. Comput. Mater. Des.*, vol. 5, no. 1, pp. 31–54, 1998.
- [28] S. I. Rao, C. Woodward, B. Akdim, E. Antillon, T. A. Parthasarathy, J. A. El-Awady, and D. M. Dimiduk, “Large-scale dislocation dynamics simulations of strain hardening of Ni microcrystals under tensile loading,” *Acta Mater.*, vol. 164, pp. 171–183, 2019.
- [29] B. Devincre, T. Hoc, and L. Kubin, “Dislocation Mean Free Paths and Strain Hardening of Crystals,” *Science (80-. )*, vol. 320, no. 5884, pp. 1745–1748, 2008.
- [30] R. Madec, B. Devincre, and L. P. Kubin, “From Dislocation Junctions to Forest Hardening,” *Phys. Rev. Lett.*, vol. 89, no. 25, pp. 1–4, 2002.

- [31] V. B. Shenoy, R. V. Kukta, and R. Phillips, “Mesoscopic analysis of structure and strength of dislocation junctions in fcc metals,” *Phys. Rev. Lett.*, vol. 84, no. 7, pp. 1491–1494, 2000.
- [32] G. P. M. Leyson, W. A. Curtin, L. G. Hector, and C. F. Woodward, “Quantitative prediction of solute strengthening in aluminium alloys,” *Nat. Mater.*, vol. 9, no. 9, pp. 750–755, 2010.
- [33] A. M. Z. Tan, C. Woodward, and D. R. Trinkle, “Dislocation core structures in Ni-based superalloys computed using a density functional theory based flexible boundary condition approach,” *Phys. Rev. Mater.*, vol. 3, no. 3, pp. 1–8, 2019.
- [34] B. Joós and M. S. Duesbery, “The peierls stress of dislocations: An analytic formula,” *Phys. Rev. Lett.*, vol. 78, no. 2, pp. 266–269, 1997.
- [35] G. Lu, N. Kioussis, V. V. Bulatov, and E. Kaxiras, “Generalized-stacking-fault energy surface and dislocation properties of aluminum,” *Phys. Rev. B*, vol. 62, no. 5, pp. 3099–3108, Aug. 2000.
- [36] D. Ferré, P. Carrez, and P. Cordier, “Modeling dislocation cores in SrTiO<sub>3</sub> using the Peierls-Nabarro model,” *Phys. Rev. B*, vol. 77, no. 1, p. 014106, Jan. 2008.
- [37] K. Kang, V. V. Bulatov, and W. Cai, “Singular orientations and faceted motion of dislocations in body-centered cubic crystals,” *Proc. Natl. Acad. Sci.*, vol. 109, no. 38, pp. 15174–15178, Sep. 2012.
- [38] C.-L. Lee and Shaofan Li, “The Size Effect of Thin Films on the Peierls Stress of Edge Dislocations,” *Math. Mech. Solids*, vol. 13, no. 3–4, pp. 316–335, May 2008.
- [39] Y. Huang, “A User-Material Subroutine Incorporating Single Crystal Plasticity in the ABAQUS Finite Element Program,” *Harvard Univ.*, no. Jun, 1991.
- [40] D. Peirce, R. J. J. Asaro, and A. Needleman, “An analysis of nonuniform and localized deformation in ductile single crystals,” *Acta Metall.*, vol. 30, no. 6, pp. 1087–1119, Jun. 1982.
- [41] G. I. Taylor, “Plastic strain in metals,” *Twenty-eighth May Lecture to the Institute of Metals*. 1938.

- [42] S. Ogata, J. Li, and S. Yip, “Ideal pure shear strength of aluminum and copper,” *Science* (80-. ), vol. 298, no. 5594, pp. 807–811, 2002.
- [43] T. H. Wille and C. Schwink, “Precision measurements of critical resolved shear stress in CuMn alloys,” *Acta Metall.*, vol. 34, no. 6, pp. 1059–1069, 1986.
- [44] S.-L. Shang, Y. Wang, T. J. Anderson, and Z.-K. Liu, “Achieving accurate energetics beyond (semi-) local density functional theory: Illustrated with transition metal disulfides,  $\text{Cu}_2\text{ZnSnS}_4$ , and  $\text{Na}_3\text{PS}_4$  related semiconductors,” *Phys. Rev. Mater.*, vol. 3, no. 1, p. 015401, Jan. 2019.
- [45] S.-L. Shang, Y. Wang, D. Kim, and Z.-K. Liu, “First-principles thermodynamics from phonon and Debye model: Application to Ni and  $\text{Ni}_3\text{Al}$ ,” *Comput. Mater. Sci.*, vol. 47, no. 4, pp. 1040–1048, Feb. 2010.
- [46] S. L. Shang, W. Y. Wang, Y. Wang, Y. Du, J. X. Zhang, A. D. Patel, and Z. K. Liu, “Temperature-dependent ideal strength and stacking fault energy of fcc Ni: a first-principles study of shear deformation,” *J. Phys. Condens. Matter*, vol. 24, no. 15, p. 155402, Apr. 2012.
- [47] D. Roylance, “The Dislocation Basis of Yield and Creep,” *Modul. Mech. Mater.*, pp. 1–15, 2001.
- [48] J. P. Hirth and J. Lothe, *Theory of dislocations*. Krieger Pub. Co, 1992.
- [49] S. L. Shang, W. Y. Wang, B. C. Zhou, Y. Wang, K. A. Darling, L. J. Kecskes, S. N. Mathaudhu, and Z. K. Liu, “Generalized stacking fault energy, ideal strength and twinnability of dilute Mg-based alloys: A first-principles study of shear deformation,” *Acta Mater.*, vol. 67, pp. 168–180, Apr. 2014.
- [50] M. Jahnatek, J. Hafner, M. Krajci, M. Jahnátek, J. Hafner, and M. Krajčí, “Shear deformation, ideal strength, and stacking fault formation of fcc metals: A density-functional study of Al and Cu,” *Phys. Rev. B*, vol. 79, no. 22, p. 224103, Jun. 2009.
- [51] S. L. Shang, Y. Wang, and Z. K. Liu, “First-principles elastic constants of alpha- and theta- $\text{Al}_2\text{O}_3$ ,” *Appl. Phys. Lett.*, vol. 90, no. 10, p. 101909, 2007.

- [52] S. L. Shang, D. E. Kim, C. L. Zacherl, Y. Wang, Y. Du, and Z. K. Liu, “Effects of alloying elements and temperature on the elastic properties of dilute Ni-base superalloys from first-principles calculations,” *J. Appl. Phys.*, vol. 112, no. 5, p. 053515, Sep. 2012.
- [53] D. Lorenz, A. Zeckzer, U. Hilpert, P. Grau, H. Johansen, and H. S. Leipner, “Pop-in effect as homogeneous nucleation of dislocations during nanoindentation,” *Phys. Rev. B*, vol. 67, no. 17, p. 172101, May 2003.
- [54] C. R. Krenn, D. Roundy, M. L. Cohen, D. C. Chrzan, and J. W. Morris, “Connecting atomistic and experimental estimates of ideal strength,” *Phys. Rev. B*, vol. 65, no. 13, p. 134111, Mar. 2002.
- [55] S.-L. Shang, Y. Wang, B. Gleeson, and Z.-K. Liu, “Understanding slow-growing alumina scale mediated by reactive elements: Perspective via local metal-oxygen bonding strength,” *Scr. Mater.*, vol. 150, pp. 139–142, Jun. 2018.
- [56] S. L. Shang, L. G. Hector Jr, Y. Wang, H. Zhang, and Z. K. Liu, “First-principles study of elastic and phonon properties of the heavy fermion compound CeMg,” *J. Phys. Condens. Matter*, vol. 21, no. 24, p. 246001, Jun. 2009.
- [57] G. Simmons and H. Wang, *Single crystal elastic constants and calculated aggregate properties: A handbook*. Cambridge: M.I.T. Press, 1971.
- [58] V. E. Osswald, “Zugversuche an Kupfer-Nickelkristallen,” *Zeitschrift für Phys. A Hadron. Nucl.*, vol. 1, no. 83, pp. 55–78, 1933.
- [59] E. N. da C. Andrade and C. Henderson, “The Mechanical Behaviour of Single Crystals of Certain Face-Centered Cubic Metals,” *Philos. Trans. R. Soc. London A*, vol. 244, no. 880, pp. 177–203, 1951.
- [60] P. S. Venkatesan and D. N. Beshers, “Plastic deformation in nickel crystals,” *Metall. Trans.*, vol. 1, no. 6, pp. 1780–1782, 1970.
- [61] E. F. Kondrat’ev and A. V. Pets, “Ferromagnetic resonance in plastically deformed nickel monocrystals,” *Sov. Phys. J.*, vol. 15, no. 2, pp. 242–244, 1972.
- [62] M. Hecker, E. Thiele, and C. Holste, “Investigation of the tensor character of mesoscopic

- internal stresses in tensile-deformed nickel single crystals by X-ray diffraction,” *Acta Mater.*, vol. 50, no. 9, pp. 2357–2365, 2002.
- [63] Y. Luo, J. Liu, W. Guo, Q. Yu, and S. Li, “Dislocation Slip Behavior of Ni Single Crystal Under Dynamic Compression,” *J. Dyn. Behav. Mater.*, vol. 2, no. 2, pp. 223–233, 2016.
- [64] Z. Yao, R. Schäublin, and M. Victoria, “Irradiation induced behavior of pure Ni single crystal irradiated with high energy protons,” *J. Nucl. Mater.*, vol. 323, no. 2–3, pp. 388–393, 2003.
- [65] A. Arsenlis and D. M. Parks, “Modeling the evolution of crystallographic dislocation density in crystal plasticity,” *J. Mech. Phys. Solids*, vol. 50, no. 9, pp. 1979–2009, Sep. 2002.
- [66] K. S. Cheong and E. P. Busso, “Discrete dislocation density modelling of single phase FCC polycrystal aggregates,” *Acta Mater.*, vol. 52, no. 19, pp. 5665–5675, 2004.
- [67] R. M. Latanision and R. W. Staehle, “Plastic deformation of electrochemically polarized nickel single crystals,” *Acta Metall.*, vol. 17, no. 3, pp. 307–319, 1969.
- [68] “Abaqus User Manual v2017,” *DS SIMULIA*, 2017.
- [69] Z. Yao, “The relationship between the irradiation induced damage and the mechanical properties of single crystal Ni,” EPFL, 2005.
- [70] J. W. Kysar, “Addendum to ‘A User-Material Subroutine Incorporating Single Crystal Plasticity in the ABAQUS Finite Element Program’, Huang, Y., Mech Report 178, Harvard University, 1991.,” *Harvard Univ. MECH Rep.*, pp. 1–3, 1997.
- [71] L. Dupuy and M. C. Fivel, “A study of dislocation junctions in FCC metals by an orientation dependent line tension model,” *Acta Mater.*, vol. 50, no. 19, pp. 4873–4885, 2002.
- [72] U. F. Kocks and H. Mecking, “Physics and phenomenology of strain hardening: The FCC case,” *Prog. Mater. Sci.*, vol. 48, no. 3, pp. 171–273, Jan. 2003.
- [73] D. Hull and D. J. Bacon, “Jogs and the Intersection of Dislocations,” in *Introduction to Dislocations*, 2011, pp. 137–155.

- [74] L. Kubin, B. Devincre, and T. Hoc, “Modeling dislocation storage rates and mean free paths in face-centered cubic crystals,” *Acta Mater.*, vol. 56, no. 20, pp. 6040–6049, 2008.
- [75] P. J. Guruprasad and A. A. Benzerga, “Size effects under homogeneous deformation of single crystals: A discrete dislocation analysis,” *J. Mech. Phys. Solids*, vol. 56, no. 1, pp. 132–156, 2008.
- [76] M. Huang, L. Zhao, and J. Tong, “Discrete dislocation dynamics modelling of mechanical deformation of nickel-based single crystal superalloys,” *Int. J. Plast.*, vol. 28, no. 1, pp. 141–158, 2012.
- [77] G. Kresse and J. Furthmüller, “Efficient iterative schemes for ab initio total-energy calculations using a plane-wave basis set,” *Phys. Rev. B*, vol. 54, no. 16, pp. 11169–11186, Oct. 1996.
- [78] G. Kresse and D. Joubert, “From ultrasoft pseudopotentials to the projector augmented-wave method,” *Phys. Rev. B*, vol. 59, no. 3, pp. 1758–1775, 1999.
- [79] J. P. Perdew, J. A. Chevary, S. H. Vosko, K. A. Jackson, M. R. Pederson, D. J. Singh, and C. Fiolhais, “Atoms, molecules, solids, and surfaces: Applications of the generalized gradient approximation for exchange and correlation,” *Phys. Rev. B*, vol. 46, no. 11, pp. 6671–6687, Sep. 1992.
- [80] M. Methfessel and A. T. Paxton, “High-precision sampling for Brillouin-zone integration in metals,” *Phys. Rev. B*, vol. 40, no. 6, pp. 3616–3621, Aug. 1989.
- [81] T. Bučko, J. Hafner, and J. G. Ángyán, “Geometry optimization of periodic systems using internal coordinates,” *J. Chem. Phys.*, vol. 122, no. 12, p. 124508, Mar. 2005.
- [82] Y. Wang, J. J. Wang, W. Y. Wang, Z. G. Mei, S. L. Shang, L. Q. Chen, and Z. K. Liu, “A mixed-space approach to first-principles calculations of phonon frequencies for polar materials,” *J. Phys. Condens. Matter*, vol. 22, no. 20, p. 202201, May 2010.
- [83] Y. Wang, S.-L. Shang, H. Fang, Z.-K. Liu, and L.-Q. Chen, “First-principles calculations of lattice dynamics and thermal properties of polar solids,” *npj Comput. Mater.*, vol. 2, no. 1, p. 16006, Nov. 2016.

- [84] Y. Wang, L.-Q. Chen, and Z.-K. Liu, “YPHON: A package for calculating phonons of polar materials,” *Comput. Phys. Commun.*, vol. 185, no. 11, pp. 2950–2968, Nov. 2014.
- [85] J. F. Bell, *The Physics of Large Deformation of Crystalline Solids*. Springer, 1968.
- [86] D. K. Bowen and J. W. Christian, “The calculation of shear stress and shear strain for double glide in tension and compression,” *Philos. Mag.*, vol. 12, no. 116, pp. 369–378, Aug. 1965.
- [87] R. Honeycombe, *The plastic deformation of metals*. 1968.
- [88] F. v. Göler and G. skar Sachs, “Das Verhalten von Aluminiumkrystallen bei Zugversuchen,” *Zeitschrift für Phys.*, vol. 41, no. 2–3, pp. 103–115, 1927.